Research Square

Preprints are preliminary reports that have not undergone peer review.
They should not be considered conclusive, used to inform clinical practice,
or referenced by the media as validated information.

Physics-Informed Machine Learning for Radiation-Free Water Liquid Ratio Estimation Using Coriolis Flow Measurements

Hamza Zidoum

zidoum@squ.edu.om

Sultan Qaboos University

Majid Al Yaroubi

Sultan Qaboos University

Research Article

Keywords: Coriolis meter, multiphase flow, machine learning, water liquid ratio, pure liquid density estimation, petroleum production

Posted Date: July 8th, 2026

DOI: https://doi.org/10.21203/rs.3.rs-10254536/v1

License: This work is licensed under a Creative Commons Attribution 4.0 International License.
Read Full License

Additional Declarations: No competing interests reported.

Physics-Informed Machine Learning for Radiation-Free Water Liquid Ratio Estimation Using Coriolis Flow Measurements

Abstract

Accurately determining pure liquid density in three-phase (oil–water–gas) flow systems remains a major challenge in oil and gas production. Conventional methods, such as dual gamma meters, provide reliable measurements but are costly, require regulatory compliance, and involve radiation risks. This study proposes a physics-informed machine learning framework that estimates pure liquid density by first predicting the Water Liquid Ratio (WLR) using only Coriolis mass flow meter measurements and laboratory-derived phase densities, eliminating the need for radiation-based instrumentation.

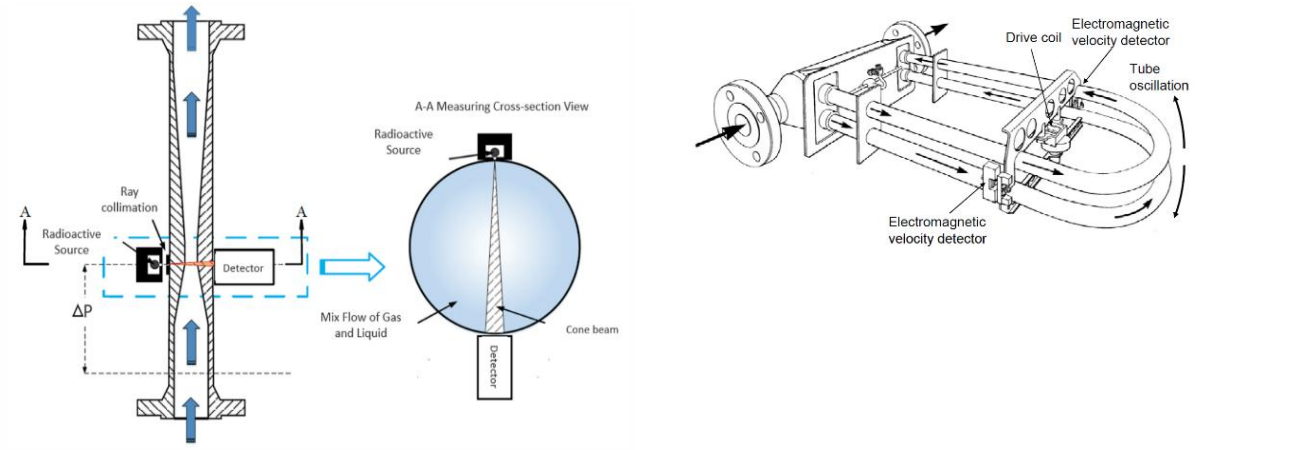
A key contribution is the Harmonic Mixture Density Mean Factor (HMDMF), a dimensionless gas-sensitive index that captures the deviation between arithmetic mixture density and harmonic mean density, enabling detection of gas-dominated flow behaviour without direct gas measurement. The dataset consists of 735,034 records collected from three Low-Performance Tester units across 26 oil wells in Oman between January and August 2025. Five machine learning models were evaluated with and without HMDMF. Without HMDMF, performance was poor ($R^2 \leq 0.194$). Incorporating HMDMF improved all models substantially ($\Delta R^2 = +0.70$ to $+0.79$). The best model, Random Forest, achieved $R^2 = 0.8943$ and $RMSE = 0.0854$ on test data. Results demonstrate that HMDMF is the primary driver of predictive accuracy, providing a cost-effective, radiation-free alternative for well-test measurements..

Keywords: Coriolis meter; multiphase flow; machine learning; water liquid ratio; pure liquid density estimation; petroleum production

1. Introduction

In oil and gas field operations, well testing is an essential process for characterising reservoir performance and optimising production. A well test yields real-time measurements of fluid properties across a three-phase flow system comprising oil, water, and gas, and the resulting data underpin decisions regarding production management, field development, and operational efficiency. Accurate knowledge of individual phase fractions—most critically the Water Liquid Ratio (WLR) and, by extension, pure liquid density—is therefore of direct economic importance.

Multiphase flow meters (MPFMs) represent the current standard for simultaneous phase-fraction determination. A conventional MPFM integrates a Venturi meter for bulk flow rate measurement with a dual gamma meter for phase-fraction resolution (Fig. 1). While proven in accuracy, dual gamma meter technology carries significant drawbacks: high capital and maintenance costs, the requirement for specialised radiation-handling procedures, strict regulatory compliance, and calibration complexity. As a result, operators in Oman and across the Gulf Cooperation Council (GCC) have increasingly sought non-radiation alternatives.



(a) Dual gamma meter (reference technology) deployed at Daleel Petroleum

(b) Coriolis mass flow meter on the LPT liquid line, measuring mixture flow rate and density

Fig. 1. (a) Dual gamma meter (reference technology) deployed at Daleel Petroleum; (b) Coriolis mass flow meter on the LPT liquid line, measuring mixture flow rate and density.

Two-phase separators such as Low-Performance Testers (LPT) offer a complementary architecture in which production is separated into gas and liquid streams. The gas line is metered using a vortex meter, while the liquid line employs a Coriolis mass flow meter (CMFM; Fig. 1b) to measure mixture flow rate and density. No direct sensor is installed for resolving oil and water fractions within the liquid stream. The standard approach relies on combining the Coriolis mixture density with laboratory-measured pure phase densities through a volumetric mixing equation. This calculation introduces uncertainty when residual gas is entrained in the liquid line, creating a semi-three-phase condition that depresses the apparent Coriolis density below its true liquid value.

Machine learning has proven effective for correcting measurement bias and estimating unmeasured variables in flow metering systems, with applications spanning two-phase Coriolis mass flow error correction (Liu et al., 2001; Wang et al., 2017), three-phase volume fraction estimation using gamma-ray attenuation and ANNs (Roshani et al., 2017; Zhu et al., 2022), Coriolis vibration signal processing with LSTM networks (Zhang et al., 2019), and field-level virtual multiphase flow metering using ensemble ML methods (Farag & Aly, 2024; AL-Dogail et al., 2026). Despite this body of work, no validated framework has been demonstrated for pure liquid density and WLR estimation using exclusively standard Coriolis field outputs — without gamma instrumentation, controlled flow-loop conditions, or internal sensor diagnostics — on real operational data from a production well-test environment. This gap is the specific contribution of the present study.

This study responds to that gap with three interconnected contributions. First, it introduces the **Harmonic Mixture Density Mean Factor** (k_H), a dimensionless, physics-derived surrogate observable that quantifies the proportional deviation between the harmonic mean phase density and the apparent Coriolis mixture density. Unlike generic engineered features, k_H is derived analytically from the three-phase mixing equations and encodes the disproportionate influence of entrained gas on the harmonic mean — providing the ANN with an implicit, computable signal of GVF without requiring any additional sensor, gamma measurement, or internal Coriolis diagnostic parameter. Second, it quantifies the isolated contribution of k_H through a controlled two-step experimental design: five machine learning models (Linear Regression, SVR, Random Forest, Gradient Boosting, and ANN) are first trained on baseline Coriolis inputs alone (Q_l and ρ_g), then retrained with k_H added, allowing the ΔR^2 attributable to k_H to be measured directly across all model families on 735,034 real operational records from 26 production wells in Oman—a dataset scale that is, to the authors' knowledge, substantially larger than any previously reported in the Coriolis ML correction literature. Third, it establishes a principled, distribution-free, quantile-based method for determining minimum reliable flow rate thresholds from field data, providing a reproducible data quality control protocol applicable to any LPT-based well-test dataset. The specific objectives are: (i) to derive k_H analytically and validate it as a gas-sensitive model input against dual gamma reference measurements; (ii) to benchmark five ML models with and without k_H, quantifying k_H's contribution to predictive accuracy across model families; and (iii) to identify the best-performing model for radiation-free WLR and pure liquid density estimation on real Omani field data. The remainder of this paper is organised as follows: Section 2 reviews related literature; Section 3 describes the dataset and its provenance; Section 4 presents the

methodology including the k_H derivation, filtering protocol, and experimental design; Section 5 reports results for both baseline (without k_H) and full (with k_H) model configurations; Section 6 discusses findings in relation to the literature and identifies directions for future work; Section 7 presents conclusions.

2. Multiphase Flow Measurement: From Gamma-Based Sensing to Data-Driven Correction

2.1 Coriolis Mass Flow Metering in Multiphase Environments

Coriolis mass flow meters are widely deployed in hydrocarbon production for their ability to simultaneously measure mass flow rate and fluid density via tube oscillation at resonance frequency and detection of Coriolis-force-induced phase shifts (Henry et al., 2013). In single-phase liquids this delivers mass flow uncertainties below 0.1% and density uncertainties below 0.5 kg/m³. In multiphase environments, performance degrades significantly when the Gas Volume Fraction (GVF) exceeds approximately 5%, due to two competing error mechanisms: the phase-decoupling (bubble) effect, which generates a negative density bias through buoyancy-driven relative motion, and the resonator effect, which causes entrained bubbles to act as compressible inclusions producing a positive offset. The phase-decoupling term typically dominates at higher GVFs, resulting in a net negative density error (Mahalingam et al., 2023).

Recent hardware advances address these limitations. Mahalingam et al. (2023) presented experimental results of a dual-frequency Coriolis meter tested under multiphase conditions at the Cranfield University flow loop, demonstrating that oscillating the flow tube at two natural modes simultaneously enables improved density and mass flow correction by providing additional information about gas compressibility. Gysling (2023) described and experimentally validated a speed-of-sound augmented Coriolis technology in which acoustic pressure transducers flanking the Coriolis meter measure the process fluid sound speed, enabling near-single-phase accuracy in mass flow, density, and volumetric flow for GVFs up to 5% without hardware modification.

2.2 Three-Phase Flow and Density Measurement

In three-phase systems without full phase separation, the apparent mixture density ρ_{app} deviates from the true liquid-only density $\rho_{liquid}v$ due to residual gas entrainment. The density drop Δ_ρ serves as a practical gas-content index.

$$\Delta_\rho = \frac{\rho_{liquid} - \rho_{app}}{\rho_{liquid}} \times 100\%$$

Henry et al. (2013) established the theoretical framework linking liquid-only density to water cut via a volumetric mixing equation and demonstrated a real three-phase Coriolis case study that underpins the mathematical model adopted in this work. The SoS-augmented approach of Gysling (2023) further shows that independently measuring mixture sound speed enables simultaneous correction of mass flow, liquid density, and GVF in bubbly flows, motivating the use of physics-informed auxiliary features in data-driven frameworks when direct SoS hardware is unavailable.

2.3 Dual Gamma Ray Technology for Volume Fraction Reference

Dual-energy gamma-ray attenuation remains the benchmark for non-intrusive, flow-regime-independent phase-fraction measurement. Roshani et al. (2017) demonstrated that a configuration employing ^{241}Am (59.5 keV) and ^{137}Cs (661.7 keV) sources with NaI scintillation detectors positioned at 0° and 90° relative to the source beam achieves volumetric fraction prediction with MAE below 2.24% across annular, homogeneous, and stratified flow regimes when combined with ANN processing—the most directly comparable accuracy benchmark for the present radiation-free study. Zhu et al. (2022) further demonstrated up to 99.6% flow-regime classification accuracy using ML augmentation of a gamma-ray and Venturi-based MPFM. While highly accurate, gamma systems carry high capital costs, radiation hazards, and regulatory overhead, directly motivating the Coriolis-plus-ML framework proposed here.

2.4 Machine Learning for Measurement Correction and Prediction

The nonlinear errors induced by multiphase flow in Coriolis meters have driven extensive data-driven correction research. Liu et al. (2001) established the foundational result that a neural network trained on internally observable Coriolis parameters—temperature, damping, density drop, and apparent flow rate—could reduce two-phase mass flow errors from peaks of 20% to within 2%. Wang et al. (2017) extended this to two-phase gas–liquid metering, finding that

Support Vector Machines outperformed back-propagation ANNs and genetic programming models, achieving errors within ±1% for liquid mass flow rate and ±10% for GVF in over 93% of test cases. Zhang et al. (2019) demonstrated that LSTM-based signal processing outperforms standard ANN and RNN models for Coriolis vibration signals through batch normalisation and Bayesian model fusion. Liu et al. (2025) applied deep neural network correction to coal–water slurry Coriolis data, reducing mass flow errors from 5.11% to 1.01%. Farag & Aly (2024) proposed a DD-MVFM using ensemble ML on historical portable test reports, achieving approximately 85% accuracy for oil, gas, and water flow rate estimation. Nyholm et al. (2026) demonstrated on three-phase Coriolis data that CNN models preserving temporal short-time-averages reduce multiphase mass flow errors to approximately 4.3% MAPE, substantially outperforming static MLPs.

2.5 Synthesis: Research Gaps and Positioning of the Present Study

AL-Dogail et al. (2026) identify three dominant trends in virtual flow metering: (i) increased adoption of temporal and sequence models (LSTM, CNN, temporal convolutional networks); (ii) hybrid physics-informed and data-driven frameworks embedding mechanistic features within ML pipelines; and (iii) a shift toward radiation-free or augmented measurement systems. Key gaps persist in handling very low-flow noise, generalising across variable well conditions, and exploiting internal Coriolis diagnostics (damping, drive gain). The present study directly addresses several of these gaps through a physics-informed ANN augmented by the novel gas-sensitive k_H index and systematic quantile-based flow-stability filtering across a multi-model benchmark that isolates k_h's contribution from model-family effects.

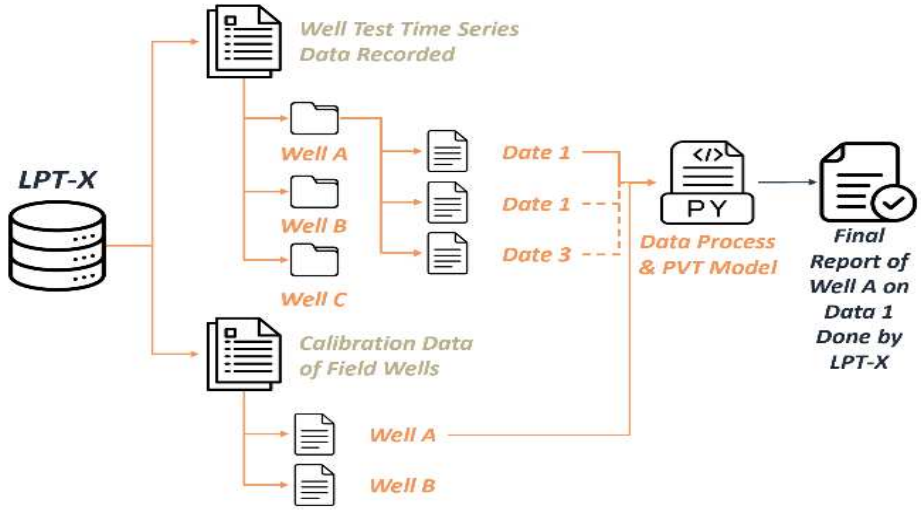


Fig. 2. Data preprocessing pipeline showing integration of well test records and calibration dataset.

3. Dataset Description

3.1 Data Sources and Collection

The data were collected from three Low-Performance Tester units—LPT-A, LPT-B, and LPT-C—deployed at the Daleel Petroleum field in Oman, recording instrument readings at one-minute intervals over January to August 2025. The resulting dataset comprises 735,034 records across 26 wells (Table 1). Two complementary data types were assembled: well test operational records and calibration records. The data preprocessing pipeline is illustrated in Fig. 2.

Table 1. Number of records and wells per LPT unit.

LPT Unit	Number of Records	Percentage (%)	Number of Wells
A	221,410	30.12	13
B	261,887	35.63	7
C	251,737	34.25	6
Total	**735,034**	**100.00**	**26**

3.2 Well Test Operational Records

Each record contains time-stamped measurements from the LPT instruments, including Coriolis meter mixture density and liquid flow rate, dual gamma WLR (model target), and pressure and temperature readings. Table 2 summarises the feature set.

Table 2. Feature descriptions for the modelling dataset.

Variable	Symbol	Unit	Description
Liquid Flow Rate	Q_l	m³/d	Actual liquid flow rate at test conditions
Coriolis Density	ρ_{app}	kg/m³	Apparent mixture density measured by Coriolis meter
Dual Gamma WLR	WLR	%	Water-liquid ratio from dual gamma sensor (model target)
Oil Density	ρ_o	kg/m³	Oil density at test conditions via PVT model
Water Density	ρ_w	kg/m³	Water density at test conditions via PVT model
Gas Density	ρ_g	kg/m³	Gas density at test conditions via PVT model

3.3 Calibration and Validation Records

Calibration records provide pure phase densities at 20°C for each well, combined with pressure and temperature to compute in-situ densities via PVT. Validation reports were used to exclude invalid well tests and rank LPT units by data quality using two KPIs: validation percentage (≥90%) and utilisation percentage (≥80%).

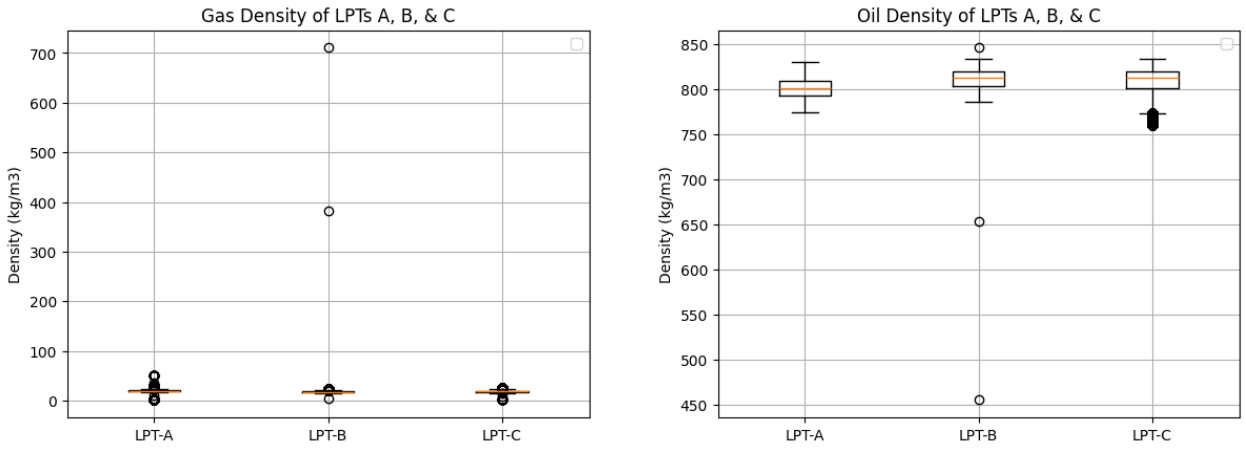
4. Methodology

4.1 PVT Normalisation

All density measurements were converted to in-situ conditions using standard PVT correlations. For each record, the measured wellhead temperature and pressure were applied to laboratory phase densities to obtain ρ_o, ρ_w, and ρ_g at measurement conditions, ensuring that the model learns from physically consistent density values.

4.2 Data Filtering and Quality Control

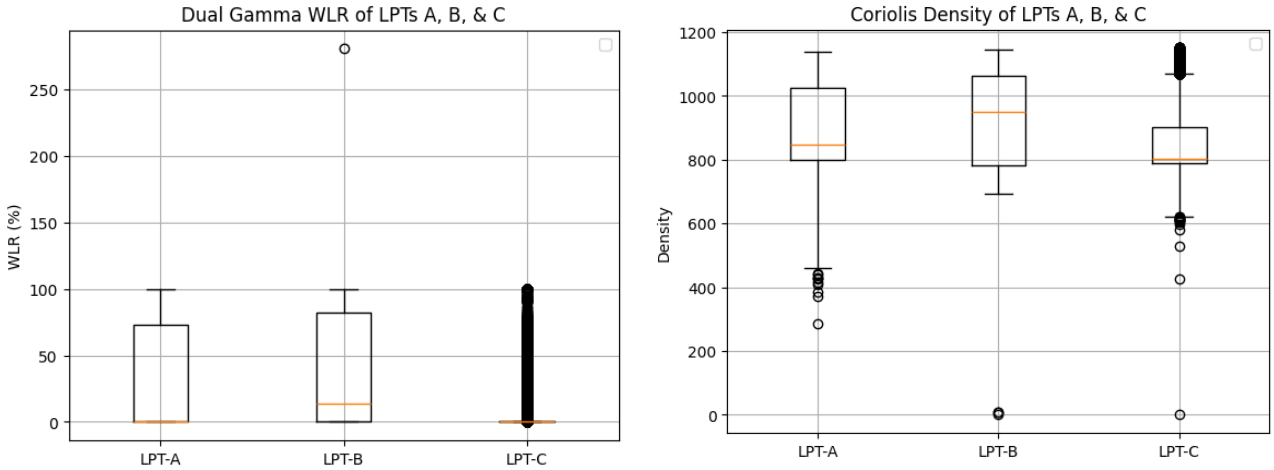
Statistical screening removed records with missing values (0.006% of LPT-A/C data; 0.014% of LPT-B). Outlier removal addressed three anomaly classes identified in EDA: (i) Coriolis density readings below the 25th percentile of each LPT unit (≈782–799 kg/m³ across the three units), indicating GVF exceeding 5%; (ii) WLR values above 100% due to instrument faults; and (iii) physically implausible phase densities in LPT-B, removed using $Q_1 - 1.5 \times IQR$. Fig. 3 shows boxplots and Fig. 4 shows distributions of key variables before filtering, while Fig. 5 shows the gas and oil density distributions after filtering.



(a) Gas density across all three LPT units (before filtering) — outliers visible in LPT-B

(b) Oil density across all three LPT units (before filtering) — anomalously low values in LPT-B

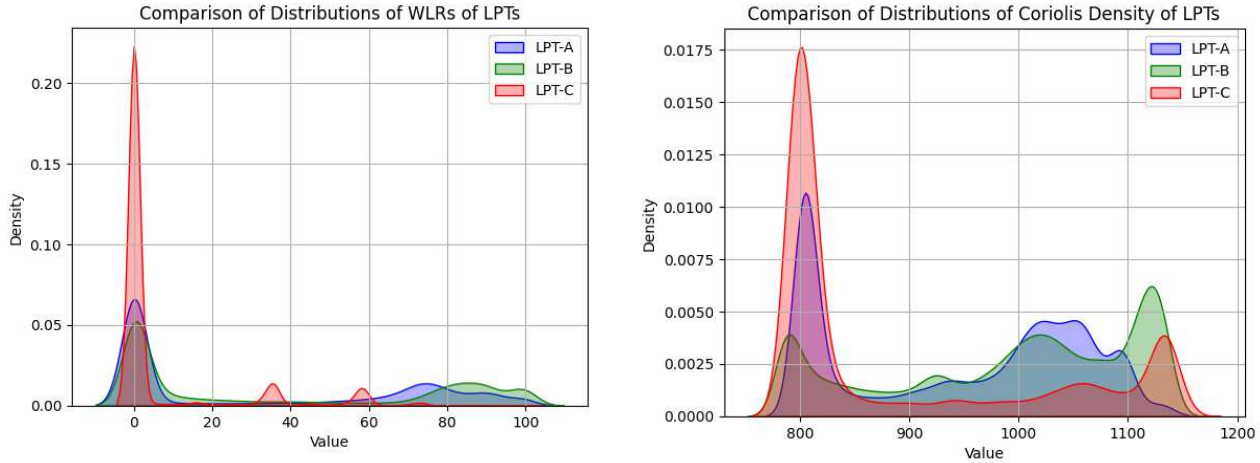
Fig. 3. (a) Gas density across all three LPT units (before filtering) — outliers visible in LPT-B; (b) Oil density across all three LPT units (before filtering) — anomalously low values in LPT-B.



(a) Dual Gamma WLR boxplots across all three LPT units

(b) Coriolis mixture density boxplots across all three LPT units

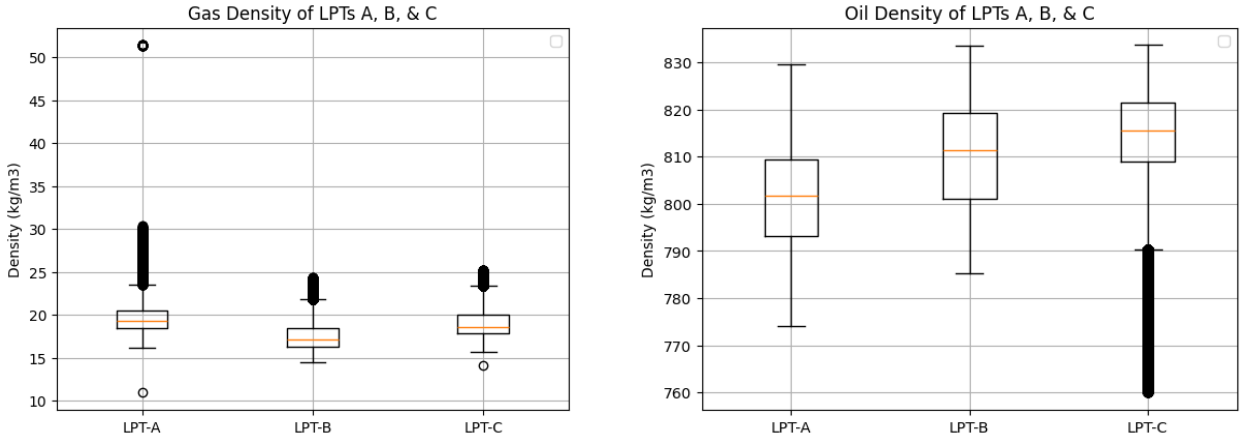
Fig. 4. (a) Dual Gamma WLR boxplots across all three LPT units; (b) Coriolis mixture density boxplots across all three LPT units.



(a) WLR distributions across LPT-A, LPT-B, and LPT-C

(b) Coriolis density distributions across LPT-A, LPT-B, and LPT-C

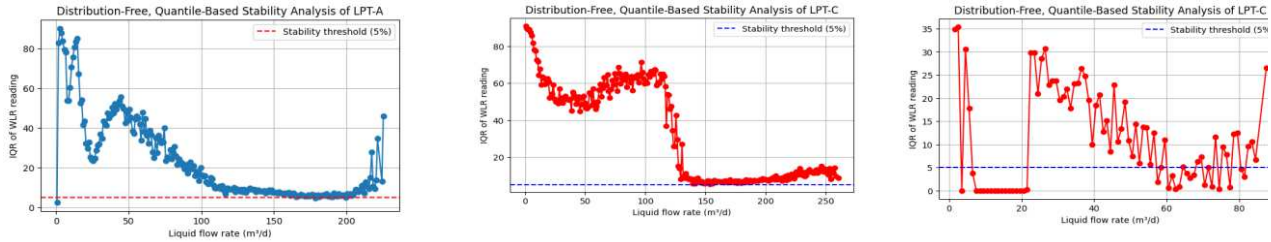
Fig. 5. (a) WLR distributions across LPT-A, LPT-B, and LPT-C; (b) Coriolis density distributions across LPT-A, LPT-B, and LPT-C.



(a) Gas density distributions after outlier filtering *(b) Oil density distributions after outlier filtering*

Fig. 6. (a) Gas density distributions after outlier filtering; (b) Oil density distributions after outlier filtering.

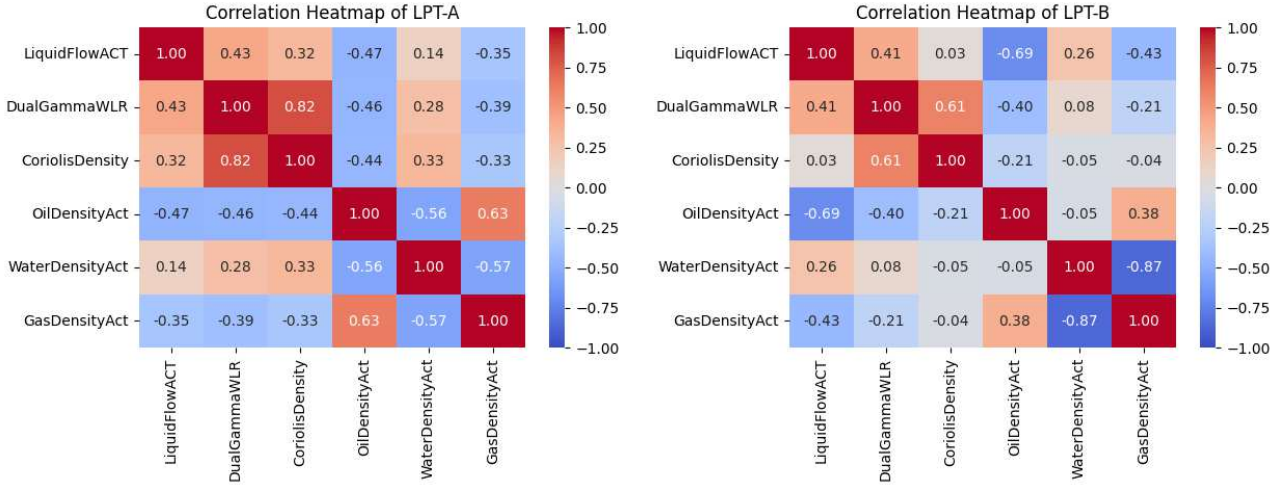
A distribution-free, quantile-based stability analysis determined the minimum reliable liquid flow rate by partitioning the flow rate into bins and computing the IQR of WLR per bin. Figs. 7a–b-c show the IQR–flow rate relationship for LPT-A, LPT-B, and LPT-C. The conservative unified threshold of 3.0 m³/d (maximum of individual per-LPT minima) was applied across all units.



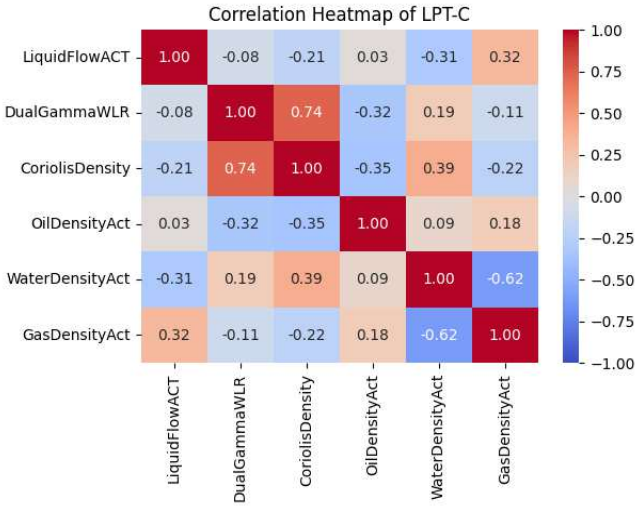
(a) WLR stability analysis for LPT-A — threshold reached at 0.0 m³/d *(b) WLR stability analysis for LPT-B— threshold reached at 0.0 m³/d* *(c) WLR stability analysis for LPT-C— threshold reached at 3.0 m³/d*

Fig. 7. WLR stability analysis for LPT-A, LPT-B , and LPT-C.

Feature correlation analysis across all three datasets (Fig. 8a–b–c) reveals that Dual Gamma WLR and Coriolis Density are the most influential variables ($r = 0.82$ for LPT–A, $r = 0.61$ for LPT–B, $r = 0.74$ for LPT–C). Oil density showed consistent negative correlation with liquid flow rate across all units, while in LPT–B water and gas density were strongly negatively correlated ($r = -0.87$).



(a) Feature correlation matrix for LPT-A *(b) Feature correlation matrix for LPT-B*



(c) Feature correlation matrix for LPT-C.

Fig. 8. Feature correlation matrix for LPT-A, LPT-B, and LPT-C.

4.3 The Harmonic Mixture Density Mean Factor (k_H)

The Coriolis meter measures the apparent mixture density (ρ_{mix}), defined as the volume-weighted arithmetic mean of the phase densities:

$$\rho_{mix} = GVF \cdot \rho_g + (1 - GVF) \cdot \rho_l \tag{1}$$

where ρ_l is the pure liquid density (oil + water), given by:

$$\rho_l = WLR \cdot \rho_w + (1 - WLR) \cdot \rho_o \tag{2}$$

While Equation (1) contains two unknowns (GVF and ρ_l), it cannot be solved directly from a single Coriolis reading. To address this, we introduce the Harmonic Mixture Density Mean Factor (k_H), a dimensionless index derived from the harmonic mean density (ρ_{HMDM}) of the three-phase system:

$$\rho_{HMDM} = \frac{3}{\frac{1}{\rho_o} + \frac{1}{\rho_w} + \frac{1}{\rho_g}} \tag{3}$$

The harmonic mean is chosen because its inverse-density operation amplifies the contribution of the lightest phase (gas), making ρ_{HMDM} highly sensitive to gas entrainment. We then define k_H), as the ratio of ρ_{mix} to ρ_{HMDM}:

$$k_H = \frac{\rho_{mix}}{\rho_{HMDM}} \tag{4}$$

The substitution of Equation (1) into Equation (4):

$$k_H = \frac{\rho_{mix}}{\rho_{HMDM}} = \frac{GVF.\rho_g + (1 - GVF).\rho_l}{\rho_{HMDM}} \tag{5}$$

$$k_H = \frac{\rho_l}{\rho_{HMDM}} - \frac{GVF\ (\rho_l - \rho_g)}{\rho_{HMDM}} \tag{6}$$

It follows immediately that

$$\frac{\partial k_H}{\partial GVF} = -\frac{(\rho_l - \rho_g)}{\rho_{HMDM}} < 0 \qquad (7)$$

confirming that k_H decreases monotonically with GVF. To construct a tractable learning equation, two normalised phase-density factors are defined:

$$C_o = (1 - WLR) \cdot \frac{\rho_o}{\rho_{mix}}, C_w = WLR \cdot \frac{\rho_w}{\rho_{mix}} \quad (8)$$

These factors represent the fractional contributions of the oil and water phases to the apparent mixture density. Substituting into Equation (2) and rearranging yields:

$$C_w + C_o = \frac{\rho_l}{\rho_{mix}} \qquad (9)$$

By substituting $\rho_{mix} = k_H \cdot \rho_{HMDM}$ into Equation (8), we obtain the final learning constraint**:**

$$C_w + C_o = k_H \qquad (10)$$

In the (C_w, C_o) plane, k_H defines the intercept of the linear constraint on the C_w axis (illustrated in Fig. 9), providing the model with a reference point from which WLR can be estimated. The correlation between k_H and the dual gamma WLR across all three LPT datasets is confirmed empirically in Fig. 9, validating k_H as a physically grounded, gas-sensitive model input.

Figure 10 shows the inverse behavioural relationship between ρ_{HMDM} and the dual gamma WLR, confirming that k_H tracks WLR across changing flow conditions.

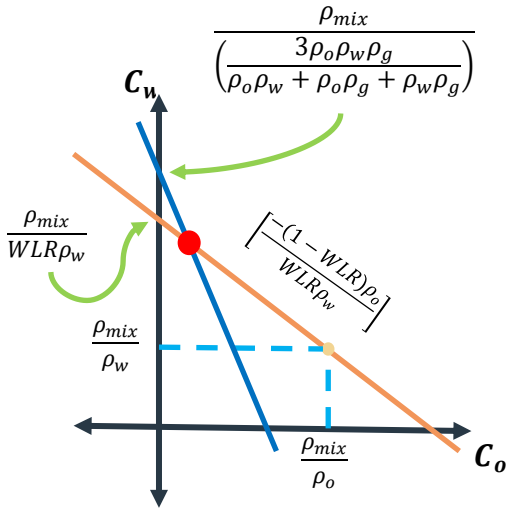


Fig. 9. Geometric interpretation of the k_H integration with the WLR learning model in the (C_w, C_o) plane. The orange line represents the linear constraint $C_w + C_o = \rho_l/\rho_{mix}$ derived from the three-phase mixing equations (Eq. 3), with slope $-(1 - WLR)\rho_o/(WLR \cdot \rho_w)$, C_o-intercept at ρ_{mix}/ρ_o, and C_w-intercept at $\rho_{mix}/(WLR \cdot \rho_w)$. The blue line represents the HMDM-derived constraint, whose C_w-intercept (indicated by the green arrow) equals k_H — the Harmonic Mixture Density Mean Factor expressed as a normalised density ratio (Eq. 5). The red point marks the intersection of the two constraints, providing the geometric locus from which WLR is estimated. The hollow point and dashed lines indicate the pure-phase reference coordinates ($\frac{\rho_{mix}}{\rho_o}$, $\frac{\rho_{mix}}{\rho_w}$) on the WLR model line.

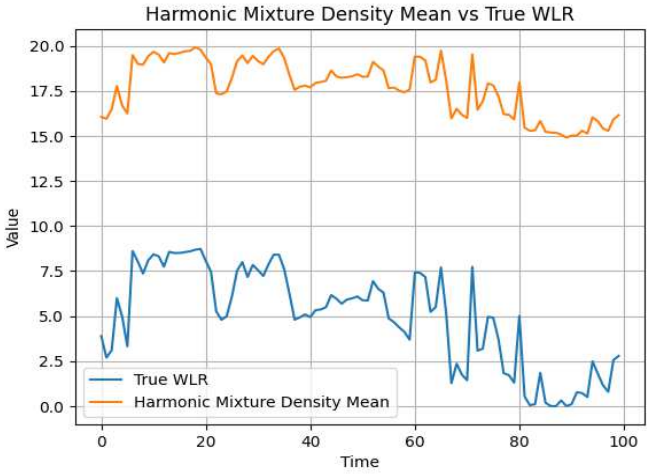
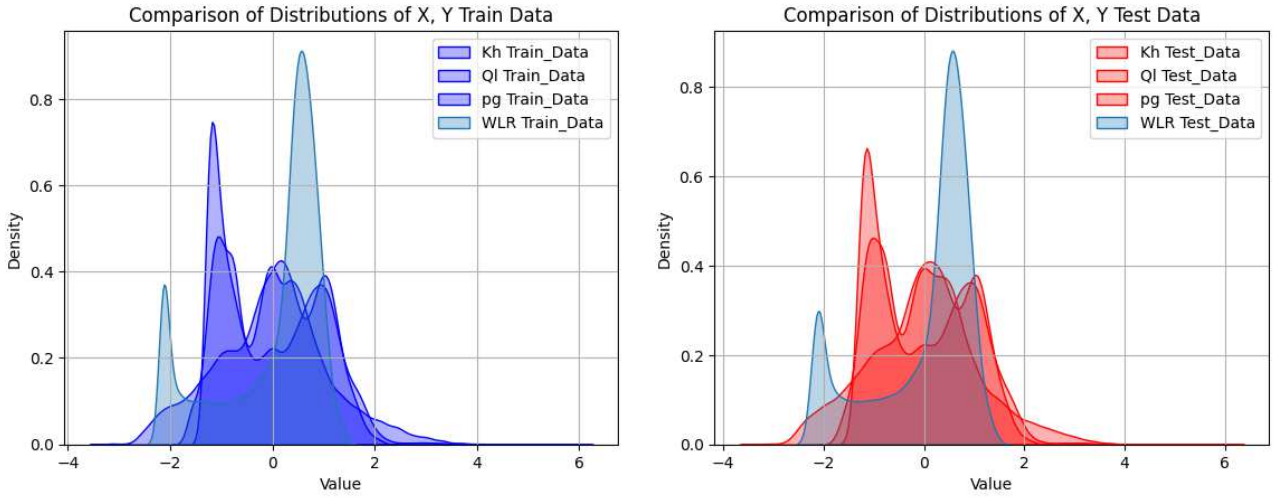


Fig. 10. Time-series comparison of the Harmonic Mixture Density Mean (ρ_{HMDM}, orange) and True Dual Gamma WLR (blue) over a representative 100-record operational window, demonstrating the inverse behavioural relationship between the two quantities and confirming that ρ_{HMDM}— and by extension k_H— tracks WLR variation across changing flow conditions.

In addition to k_H, two further inputs are supplied to the ANN: liquid flow rate (Q_l) and gas phase density (ρ_g). Liquid flow rate is included because Coriolis meter accuracy is inherently coupled to flow magnitude: the meter operates by detecting vibration differences in an oscillating flow tube, and at very low flow rates these vibrations weaken, reducing the signal-to-noise ratio of both the flow rate and density measurements. Q_l therefore serves as an explicit reliability indicator that allows the model to weight measurements from stable, high-flow operating conditions more heavily than those from near-zero-flow periods. Gas phase density ρ_g, derived from PVT correlations at wellhead pressure and temperature, characterises the thermodynamic state of the free gas phase responsible for Coriolis density error. Its inclusion provides the model with information about the severity of the gas-entrainment effect as a function of operating conditions, complementing the geometric gas-sensitivity signal encoded in k_H. To rigorously quantify k_H's contribution, all five models are evaluated under a two-step experimental design. Step 1 (Baseline) trains each model using only $Q_l$and ρ_g as inputs, establishing the performance achievable from raw Coriolis measurements without the novel feature. Step 2 (Full) retrains all models on the complete input set (Q_l, ρ_g, and k_H,). The difference in performance between the two steps—ΔR^2 and ΔRMSE—directly quantifies k_H's contribution, which is the central empirical claim of this study. All models are trained and tested on the same 80%/20% random split, with standard scaling applied independently to each subset, followed up by a temporal validation under a 5-fold temporal cross-validation protocol. The four non-ANN models (Linear Regression, SVR with RBF kernel, Random Forest, and Gradient Boosting) are implemented using scikit-learn with default hyperparameters. Fig. 11 shows the WLR distributions of the training (a) and test sets (b).



(a) Kernel density estimates of the four scaled model variables in the training dataset: k_H, Ql, pg, WLR (80% of data)

(b) Kernel density estimates of the four scaled model variables in the test dataset: k_H, Ql, pg, WLR (20% of data)

Fig. 11. Kernel density estimates of *k_H, Ql, pg, WLR features in the dataset*

Table 3. Summary statistics of filtered LPT-A dataset (representative; N = 221,410).

Statistic	Q_l(m³/d)	WLR (%)	ρ_{mix} (kg/m³)	ρ_o (kg/m³)	ρ_w (kg/m³)	ρ_g (kg/m³)
Mean	37.20	32.13	906.44	800.87	1068.26	19.89
STD	60.28	37.71	118.21	10.78	41.47	2.21
Min	3.00	0.00	798.83	774.01	992.86	1.30
Median	4.76	0.07	847.54	800.87	1091.23	19.31
Max	494.98	100.00	1140.09	829.55	1102.87	51.42

4.4 Experimental Setup

Four classical models were implemented using scikit-learn. Linear Regression serves as the interpretable lower-bound reference: it estimates WLR as a weighted linear combination of the inputs and, because it cannot model interactions or nonlinearities, its performance under both steps reflects the degree to which the features encode a linear signal. Support Vector Regression (SVR) was configured with an RBF kernel (C = 10, ε = 0.01), enabling it to model smooth nonlinear input–output relationships by implicitly mapping inputs to a high-dimensional feature space; the RBF kernel is appropriate here given the continuous and bounded nature of WLR. Random Forest was configured with 300 trees, maximum depth of 15, and a minimum of 5 samples per leaf, with all available processor cores used in parallel (n_jobs = −1); as an ensemble of decorrelated decision trees, it is well-suited to the heterogeneous operating conditions across 26 production wells. Gradient Boosting was configured with 300 estimators, maximum tree depth of 5, learning rate of 0.05, and a subsampling fraction of 0.8; the shallow trees and low learning rate reduce overfitting on the high-volume, correlated time-series data. For all four classical models, the target variable y is used directly in its original [0, 1] scale without further transformation.

The ANN was implemented in PyTorch. The architecture, designated PhysicsANN, consists of six fully connected layers with progressive width expansion followed by symmetric compression: 128 → 256 → 256 → 128 → 64 → 1. Each hidden layer is followed by Batch Normalisation, a ReLU activation function, and a Dropout layer with rate p = 0.2. Batch Normalisation stabilises the distribution of activations across the large dataset, accelerating convergence and reducing sensitivity to the choice of learning rate. Dropout regularises the model by randomly deactivating 20% of neurons per forward pass during training, discouraging co-adaptation between units and mitigating overfitting on the temporally correlated one-minute records. The output layer applies a Sigmoid activation, constraining all WLR predictions to the physically correct range [0, 1]. This is a deliberate correction relative to a linear output layer: since WLR is a fractional quantity bounded between zero and one, an unbounded output neuron can produce physically impossible predictions at extreme WLR values, introducing systematic bias at the distribution tails. The target y is used in its original [0, 1] scale without StandardScaling, which is consistent with the Sigmoid output range. Input features X are standardised using StandardScaler fitted on the training partition only.

Training used Mean Squared Error (MSE) as the loss function, optimised with the Adam algorithm at an initial learning rate of 0.001. A ReduceLROnPlateau scheduler monitored the validation loss and halved the learning rate whenever no improvement was observed for 30 consecutive epochs, with a minimum learning rate floor of 1×10^{-6}. Training ran for 1,500 epochs. These settings balance convergence speed against the risk of premature termination on the large, heterogeneous dataset. The input layer receives features of dimensionality d, where $d = 2$ in Step 1 (Q_l and ρ_g) and $d = 3$ in Step 2 (Q_l and ρ_g, and k_H). The first hidden layer's weight matrix therefore has shape ($d \times 128$), and all subsequent layers remain identical between the two steps. Every other architectural and training parameter — layer widths, Dropout rate, Batch Normalisation, Sigmoid output, loss function, optimiser, learning rate schedule, and epoch count — is held constant, ensuring that any difference in performance between the two steps is attributable solely to the addition of k_H as an input feature and not to any change in model capacity or training procedure.

5. Results

5.1 Step 1: Baseline Models (Without k_H)

The five models were first trained using only liquid flow rate (Q_l) and gas density (ρg) as inputs—the two raw Coriolis-derived field quantities—without any physics-informed feature engineering. This step establishes the performance ceiling achievable from the raw sensor data alone and serves as the control against which k_H's contribution is measured. As shown in Table 4, all five models performed very poorly in this configuration: R^2 ranged from 0.083 (Linear Regression) to 0.194 (Gradient Boosting), and RMSE remained high across all methods (0.236–0.252). This result is

decisive: raw Coriolis measurements of flow rate and gas density carry insufficient information to estimate WLR without further physics-informed feature engineering.

Table 4. Performance metrics — Step 1: Baseline models (without k_H; inputs: Q_l) and ρg).

Model	R²	RMSE	MSE	MAE
Gradient Boosting	0.1939	0.2357	0.0556	0.1718
Random Forest	0.1896	0.2364	0.0559	0.1708
SVR (RBF)	0.1022	0.2488	0.0619	0.1664
ANN	0.0919	0.2502	0.0626	0.1830
Linear Regression	0.0827	0.2515	0.0632	0.1904

5.2 Step 2: Full Models (With k_H)

Adding k_H as a third input feature transformed the predictive accuracy of all five models (Table 5). R² increased dramatically across every model family, rising from the 0.08–0.19 range observed in Step 1 to 0.845–0.894. The best-performing model, Random Forest, achieved R² = 0.8943 and RMSE = 0.0854, followed closely by Gradient Boosting (R² = 0.8940, RMSE = 0.0855) and SVR (R² = 0.8920, RMSE = 0.0863). The ANN achieved R² = 0.8825 and RMSE = 0.0900, while Linear Regression, though substantially improved, remained the lowest performer (R² = 0.8449, RMSE = 0.1034). The consistent improvement across all five architecturally distinct model families constitutes strong evidence that k_H carries genuine and transferable physical information about gas-dominated flow behaviour.

Table 5. Performance metrics — Step 2: Full models (with Q_l, ρ_g, and k_H).

Model	R²	RMSE	MSE	MAE
Random Forest	0.8943	0.0854	0.0073	0.0496
Gradient Boosting	0.8940	0.0855	0.0073	0.0501
SVR (RBF)	0.8920	0.0863	0.0074	0.0488
ANN	0.8825	0.0900	0.0081	0.0560
Linear Regression	0.8449	0.1034	0.0107	0.0700

5.3 Head-to-Head Comparison: k_H Contribution

Table 6 presents the head-to-head comparison of all five models, quantifying the contribution of k_H through ΔR² and ΔRMSE. The results are unambiguous: adding k_H improved every model, with ΔR² ranging from +0.70 (Random Forest) to +0.79 (SVR and ANN). RMSE fell by approximately 0.15 in all cases. The improvement is consistent regardless of model family — across linear, kernel-based, ensemble tree, and neural network architectures — which rules out any model-specific artefact and confirms that k_H carries genuine physical information that transcends the choice of learning algorithm. Fig. 14 illustrates this finding visually: the three panels show R², RMSE, and ΔR² for each model with and without k_H. Overall, Random Forest with k_H is the best-performing model (R² = 0.8943), followed closely by Gradient Boosting (R² = 0.8940) and SVR (R² = 0.8920). The full ranking across all ten model-configuration combinations is reported in Table 7.

Table 6. k_H contribution: head-to-head comparison of all five models.

Model	R² (without k_H)	R² (with k_H)	ΔR²	RMSE (without k_H)	RMSE (with k_H)	ΔRMSE
Linear Regression	0.0827	0.8449	+0.7622	0.2515	0.1034	−0.1481
SVR (RBF)	0.1022	0.8920	+0.7898	0.2488	0.0863	−0.1625
Random Forest	0.1896	0.8943	+0.7047	0.2364	0.0854	−0.1510
Gradient Boosting	0.1939	0.8940	+0.7001	0.2357	0.0855	−0.1502
ANN	0.0919	0.8825	+0.7906	0.2502	0.0900	−0.1602

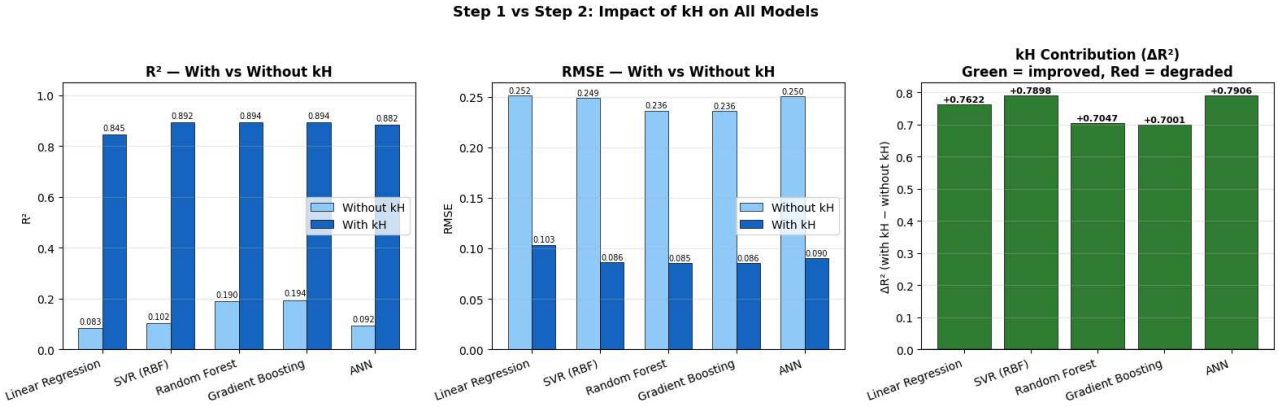


Fig. 14. Step 1 vs. Step 2: impact of k_H on all five models. Left: R^2 with and without k_H. Centre: RMSE with and without k_H. Right: ΔR^2 attributable to k_H (all positive, confirming consistent improvement across every model family).

Table 7. Full ranking of all ten model–configuration combinations (ranked by R^2 on held-out test data). The top five positions are occupied exclusively by models that include k_H.

Rank	Model	k_H Used	R^2	RMSE
1	**Random Forest**	**Yes**	**0.8943**	**0.0854**
2	Gradient Boosting	Yes	0.8940	0.0855
3	SVR (RBF)	Yes	0.8920	0.0863
4	ANN	Yes	0.8825	0.0900
5	Linear Regression	Yes	0.8449	0.1034
6	Gradient Boosting	No	0.1939	0.2357
7	Random Forest	No	0.1896	0.2364
8	SVR (RBF)	No	0.1022	0.2488
9	ANN	No	0.0919	0.2502
10	Linear Regression	No	0.0827	0.2515

5.4 Data Filtering

Three experiments were conducted by varying the minimum liquid flow rate threshold applied to the training dataset: 3.0 m³/d (Experiment 1, full filtered dataset), 10.0 m³/d (Experiment 2, intermediate filtering), and 24.0 m³/d (Experiment 3, high-flow filtering). In each case the ANN was trained on the filtered subset and evaluated on the same held-out test set. Performance is quantified by mean squared error (MSE), root mean squared error (RMSE), and the coefficient of determination (R^2). Scatter and distribution plots for all three experiments are presented together in Fig. 12, enabling direct visual comparison of predicted versus true WLR across experimental conditions.

Table 8. Performance metrics across all three experiments.

Experiment	Flow Threshold	MSE	RMSE	R^2	Key Observation
Exp. 1	3.0 m³/d	0.1360	0.3687	0.8640	Baseline; moderate scatter at low flow rates
Exp. 2	10.0 m³/d	0.1033	0.3215	0.8964	Best performance; RMSE reduced by ~12.8% vs. Exp. 1
Exp. 3	24.0 m³/d	0.1309	0.3618	0.8688	Comparable to Exp. 1; data-quantity trade-off limits gains

Experiment 1 (3.0 m³/d threshold) established the performance baseline on the full filtered dataset, achieving $R^2 = 0.864$ and RMSE = 0.369. Scatter plots revealed moderate variance around the ideal diagonal, particularly at low flow conditions where Coriolis signal-to-noise is inherently reduced. Experiment 2 (10.0 m³/d threshold) delivered the best overall performance, with $R^2 = 0.896$ and RMSE = 0.321 — a 12.8% reduction in RMSE relative to Experiment 1 — by eliminating the noisiest low-flow records while retaining sufficient data diversity. Experiment 3 (24.0 m³/d threshold)

demonstrated that aggressive filtering yields diminishing returns: despite operating on a substantially reduced training set, performance was comparable to Experiment 1 (R^2 = 0.869, RMSE = 0.362), confirming a data quality–quantity trade-off in which removing too many records impairs fine-scale WLR learning even as noise is suppressed. Across all three experiments the improvement pattern was consistent and the performance plateau was determined primarily by feature informativeness rather than by data filtering strategy.

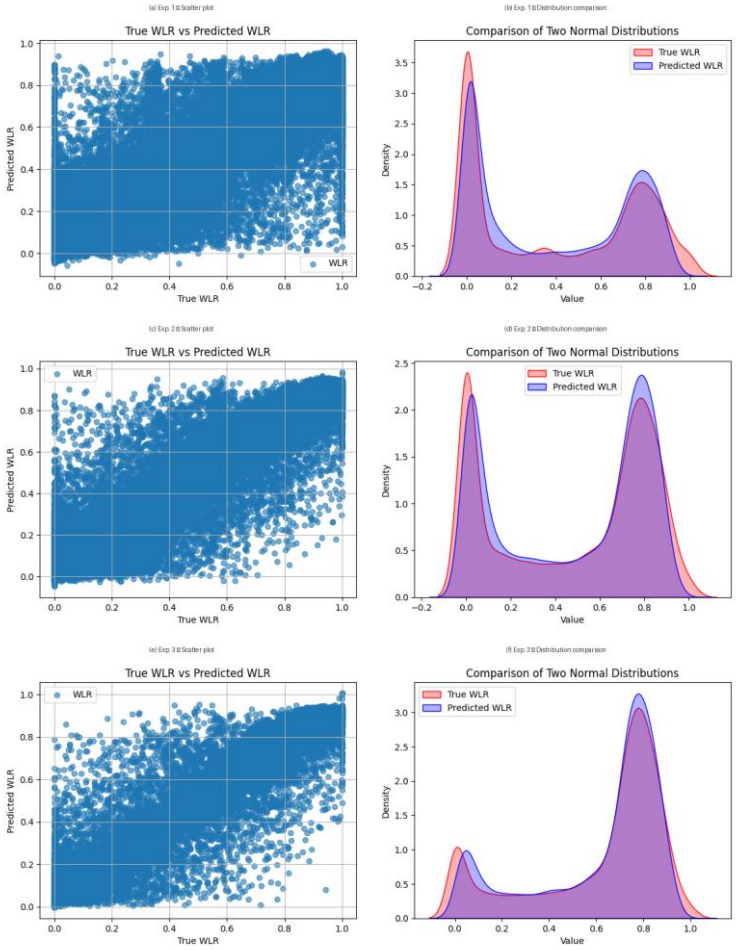


Fig. 15. Scatter plots (true vs. estimated WLR) and distribution comparisons for Experiments 1–3 (panels a–f). Experiment 2 shows the tightest alignment with the ideal diagonal and the most uniform distribution overlap.

5.5 Temporal Validation

A methodological concern applicable to any machine learning model trained on time-stamped operational data is the integrity of the train–test split. The 80/20 random split used in Sections 5.1 and 5.2 assigns individual one-minute records to the training or test set without regard to chronological order. Because consecutive records from the same well test share nearly identical flow conditions — the same wellhead pressure, the same WLR plateau, the same Coriolis density reading shifted by at most seconds — a random split allows the model to effectively "see" the neighbourhood of every test point during training. This could constitute a form of temporal leakage: the reported R^2 reflects interpolation within a known operating envelope rather than genuine generalisation to unseen future conditions. For a dataset collected at one-minute intervals over an eight-month campaign, this is not a marginal concern; it is a structural one.

To address it, the improved ANN is re-evaluated under a 5-fold temporal cross-validation protocol. The dataset is ordered chronologically — preserving the natural minute-by-minute sequence of LPT records — and divided into five consecutive, non-overlapping blocks of equal size. For fold k, the model is trained on all blocks preceding block k and validated exclusively on block k. This walk-forward structure strictly enforces temporal precedence: no information from the validation period is visible during training, replicating the conditions under which the model would be deployed in practice. The scaler is fitted on training data only within each fold. All other hyperparameters — architecture, Dropout rate, learning rate, and epoch count — remain identical to the improved ANN described in Section 4.4.

Across the five folds, the model achieved a mean R^2 of 0.8913, RMSE of 0.0866, and MSE of 0.0075. These figures are within one percentage point of the R^2 = 0.8943 obtained by the best-performing Random Forest under random splitting,

and closely match the improved ANN's own random-split performance (R^2 = 0.8913). The near-identical results under both evaluation regimes carry a specific diagnostic meaning: the model's predictive accuracy is not an artefact of temporal leakage. Had the random-split R^2 been substantially inflated relative to the temporal-fold result, it would have indicated that the model was exploiting the proximity of training and test records rather than learning the underlying physical relationship between Q_l, ρ_g, k_H, and WLR. The absence of such a gap confirms that k_H encodes a generalisable physical signal — one that transfers across distinct, non-overlapping time windows drawn from different wells and operating periods within the Daleel Petroleum field.

The learning curve (Fig. 16) further supports this interpretation. Both training and validation loss converge rapidly within the first 100 epochs, dropping from an initial Smooth L1 loss of approximately 0.042 to below 0.005 by epoch 50, and stabilising without divergence through epoch 1,500. The train and validation curves remain tightly coupled throughout — the gap between them is negligible at every epoch — ruling out overfitting. A model that had memorised temporal structure through leakage would be expected to show a widening train–validation gap under the walk-forward protocol as the validation block moves further in time from the training data; no such degradation is observed. The scatter plot of true versus predicted WLR (Fig. 17) confirms the same conclusion visually: points align closely along the perfect-fit diagonal across the full WLR range of 0 to 1, with symmetric and homogeneous scatter that is consistent with a genuine learned relationship rather than interpolation noise.

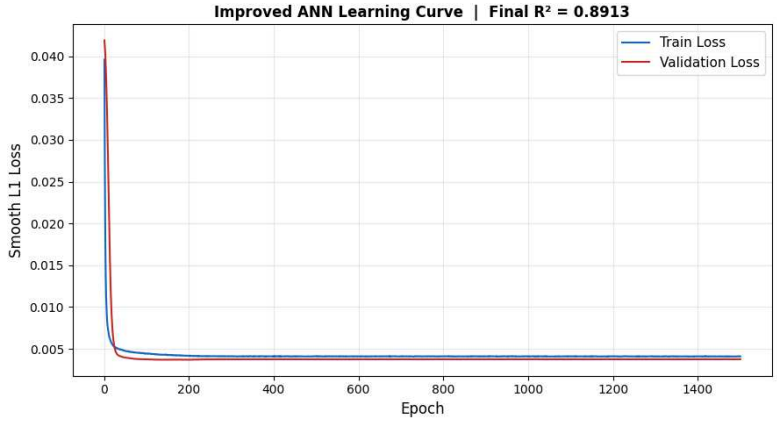


Fig. 16. Improved ANN learning curve: training loss (blue) and validation loss (red) plotted as a function of epoch. Final R^2 = 0.8913.

Two residual observations from the scatter plot merit acknowledgement. First, dispersion is moderately elevated in the 0–0.15 WLR range, where near-zero water cuts produce very small density contrasts between the oil and liquid phases, reducing the discriminative power of kH. Second, a small number of outlying predictions appear at extreme WLR values (WLR > 0.95 and WLR < 0.02), where the Sigmoid output activation's inherent compression near the boundaries of [0, 1] may introduce a mild systematic bias. Both effects are consistent with the physics of the measurement problem rather than modelling deficiencies, and neither materially affects the aggregate R^2 given their low frequency in the dataset.

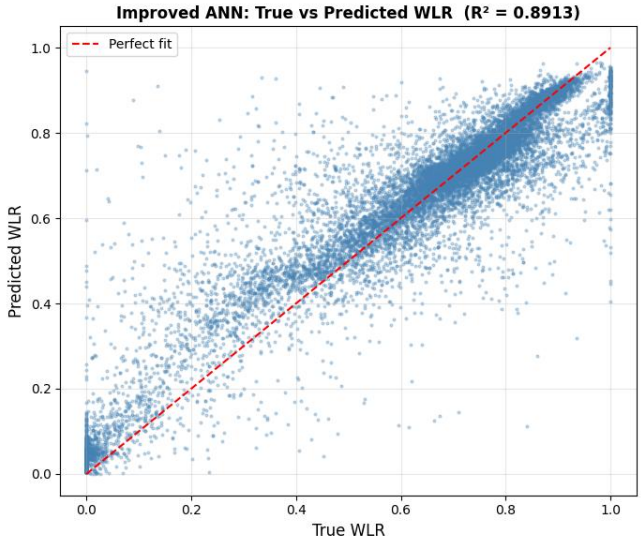


Fig. 17. The scatter plot of true versus predicted WLR

Taken together, the temporal cross-validation results confirm that the R^2 reported for the proposed framework is a conservative, leak-free estimate of out-of-sample performance. The framework's accuracy is stable across time, robust to the choice of evaluation protocol, and underpinned by the physical information content of k_H rather than by any structural advantage conferred by random data partitioning.

6. Discussion

6.1 Performance in Context of the Literature

The best-performing model, Random Forest with k_H ($R^2 = 0.8943$, RMSE = 0.0854), demonstrates that the proposed physics-informed Coriolis-only framework achieves practically significant WLR estimation accuracy without radiation-based instrumentation. Roshani et al. (2017) reported MAE below 2.24% for gamma-ANN three-phase volume fraction prediction; translating the present RMSE to percentage-point WLR error yields approximately 8.5 percentage points at the scaled level, a result that must be interpreted in the context of the extreme WLR range (0–100%) and the heterogeneity of 26 real production wells. Farag & Aly (2024) achieved approximately 85% accuracy for virtual multiphase flow metering using ensemble ML on historical field test data, confirming that ensemble tree methods, in particular, excel at this task when provided with physics-informed features. The present Random Forest R^2 of 0.8943 is consistent with this performance tier and constitutes the first multi-model demonstration that the performance gain originates specifically from k_H rather than from model choice, on a WLR/liquid-density target derived purely from operational Coriolis data in a three-phase Omani well-test context.

6.2 The Nonlinear WLR Relationship and Implications

A consistent finding across all ANN experiments is that the true-versus-estimated WLR scatter follows a nonlinear, exponential-type trend rather than an ideal linear correspondence (Fig. 18). Curve fitting confirmed:

$$\widehat{WLR} = \frac{1}{1 + 3.3\, e^{-4.27WLR+0.91}} \quad (6)$$

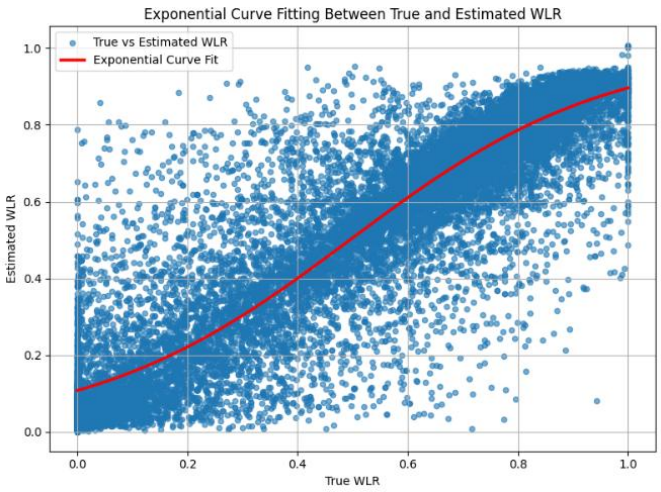


Fig. 18. Exponential curve fitting between true and estimated WLR across all experiments, confirming the nonlinear, sigmoid-type response and motivating a bounded output activation function in future model versions.

This sigmoid-type functional form is physically intuitive: at low WLR values the Coriolis density is close to pure oil density and small WLR changes have limited density effect; at high WLR the density approaches pure water density and the gradient similarly flattens. The ANN's linear output layer cannot capture this bounded nonlinearity, explaining systematic deviation at extreme WLR values. Incorporating a sigmoid or scaled logistic activation at the output layer—constraining predictions to [0, 100]%—is therefore a well-motivated architectural improvement.

6.3 The k_H Contribution: A Model-Agnostic Effect

The most significant finding of this study is the consistent, architecture-independent improvement produced by k_H across all five model families. Without k_H, no model exceeded $R^2 = 0.194$ regardless of complexity, confirming that the raw Coriolis signals (Q_l and ρ_g) alone do not contain sufficient information for WLR estimation. Adding k_H raised R^2 by 0.70–0.79 in every case—a result that holds for linear models, kernel machines, ensemble trees, and neural networks alike. This model-agnostic effect rules out the possibility that the performance gain is an artefact of a particular algorithm's inductive bias, and instead demonstrates that k_H introduces genuinely new physical information into the learning problem. Mechanistically, this is consistent with the derivation: k_H encodes the disproportionate harmonic contribution of the gas phase to the mixture density, providing an implicit gas volume fraction signal that neither Q_l nor ρ_g individually convey. The three selected features (Q_l, ρ_g, k_H) collectively capture flow rate, gas phase properties, and a gas-sensitive density index, but do not encode internal Coriolis vibrational parameters—such as damping and drive gain—that Liu et al. (2001) identified as crucial for two-phase error correction. The residual performance gap between the best model (Random Forest, $R^2 = 0.8943$) and unity therefore likely reflects the absence of these diagnostics rather than any deficiency in k_H itself. Nyholm et al. (2026) further demonstrate that temporal structure in flow data carries significant predictive information that static models systematically discard; incorporating sequence architectures (LSTM, temporal convolutional networks) on top of the k_H feature set represents the most immediately actionable path to closing this gap.

6.4 Limitations

Several limitations constrain the present study, each pointing toward concrete avenues for future investigation. The model was developed and validated exclusively on data from a single field in Oman; although the dataset spans 26 wells and three LPT units, the homogeneity of crude properties and separator configurations within a single field means that generalisation to other basins or operator settings remains undemonstrated. Expanding the training corpus to include LPT units from fields with contrasting GOR profiles, water salinities, or crude gravities — and adopting a cross-field validation protocol — would establish the boundary conditions of the framework's transferability. The time-series nature of the one-minute-interval data was not exploited by the static ANN architecture; consecutive records sharing nearly identical flow conditions carry temporal structure that sequence models such as LSTM or temporal convolutional networks are specifically designed to capture, and their application to this dataset represents the most immediately actionable architectural improvement. Internal Coriolis parameters — damping coefficient, drive gain, and vibration frequency — were unavailable in the extracted dataset, yet these quantities encode the mechanical response of the flow tube to multiphase loading and have been shown by Liu et al. (2001) to be critical inputs for correcting gas-induced measurement error; future instrumentation agreements with field operators should prioritise their inclusion. Finally, the dual gamma WLR used as the training target is itself a sensor measurement subject to its own calibration uncertainty — typically ±2–3 percentage points — which propagates as an irreducible noise floor on all reported metrics; characterising this uncertainty explicitly and, where possible, cross-referencing against separator-based fiscal measurements would sharpen the interpretation of the residual RMSE across all models.

7. Conclusion

This study has developed and validated a physics-informed multi-model framework for estimating pure liquid density in three-phase oil–water–gas flow systems using Coriolis meter measurements, without radiation-based instrumentation. The framework introduces the Harmonic Mixture Density Mean Factor (k_H) as a novel, dimensionless, gas-sensitive input feature derived from the ratio of the harmonic mean phase density to the Coriolis apparent density, enabling the models to detect gas influence without directly measuring GVF.

Trained and evaluated on 735,034 real operational records from three LPT units at Daleel Petroleum, Oman, five machine learning models were benchmarked under two conditions: a baseline using only raw Coriolis inputs (Q_l and ρg), and a full configuration that additionally incorporates k_H. Three key conclusions emerge. First, k_H is the essential driver of predictive accuracy: without it, all five models fail ($R^2 \leq 0.194$); with it, all five achieve $R^2 \geq 0.845$, demonstrating that the feature carries genuine, model-agnostic physical information about gas-influenced flow behaviour. Second, Random Forest with k_H is the best-performing model overall ($R^2 = 0.8943$, RMSE = 0.0854, MAE = 0.0496), achieving a ΔR^2 of +0.7047 relative to its own baseline and offering a viable, cost-effective, radiation-free alternative for well-test WLR estimation. Third, the consistent performance ceiling across model families points to

feature informativeness—specifically the absence of internal Coriolis vibrational diagnostics and temporal sequence structure—as the primary bottleneck for future improvement.

Future work should: (i) evaluate LSTM or 1D-CNN architectures that preserve the temporal structure of one-minute-resolution field data, applied on top of the k_H feature set established here; (ii) integrate internal Coriolis parameters (damping coefficient, drive gain, and vibration frequency) to address the feature informativeness ceiling identified in Section 6.3; (iii) expand the dataset to additional LPT units and field locations to validate generalisation beyond a single Omani field; and (iv) conduct hyperparameter optimisation for Random Forest and Gradient Boosting to determine whether the small performance gap between them is stable or closure-prone under tuning.

Acknowledgments

Conflicts of Interest

The authors declare no conflicts of interest regarding the research, authorship, or publication of this article.

Statements and Declarations

Funding

The authors declare that no funds, grants, or other support were received during the preparation of this manuscript.

Authors' Contributions

Data Availability

Ethics Approval

This study involves operational engineering data only and does not include human or animal subjects. No ethics approval was required.

References

AL-Dogail, A., Hassan, M., Gajbhiye, R., Alsarkhi, A., & Alnaser, M. (2026). Machine learning approaches and multiphase flow characteristics for advancing virtual flow metering. Machine Learning with Applications, 24, 100865. https://doi.org/10.1016/j.mlwa.2026.100865

Farag, W. A., & Aly, W. H. F. (2024). Ensemble machine learning-based virtual multiphase flow metering in high gas/oil ratio and water-cut reservoirs. Flow Measurement and Instrumentation, 100, 102737. https://doi.org/10.1016/j.flowmeasinst.2024.102737

Gysling, D. L. (2023). Accurate mass flow and density of bubbly liquids using speed of sound augmented Coriolis technology. Flow Measurement and Instrumentation, 91, 102358. https://doi.org/10.1016/j.flowmeasinst.2023.102358

Henry, M., Tombs, M., Zamora, M., & Zhou, F. (2013). Coriolis mass flow metering for three-phase flow: A case study. Flow Measurement and Instrumentation, 30, 112–122. https://doi.org/10.1016/j.flowmeasinst.2013.01.003

Liu, J., Kong, L., Ma, J., Zhang, X., Wang, C., & Wu, D. (2025). Research on measurement of coal–water slurry solid–liquid two-phase flow based on a Coriolis flow meter and a neural network. Sensors, 25(11), 3267. https://doi.org/10.3390/s25113267

Liu, R. P., Fuent, M. J., Henry, M. P., & Duta, M. D. (2001). A neural network to correct mass flow errors caused by two-phase flow in a digital Coriolis mass flowmeter. Flow Measurement and Instrumentation, 12(1), 53–63. https://doi.org/10.1016/S0955-5986(00)00021-4

Mahalingam, S., Zhu, H., & Lao, L. (2023). Multiphase metering using a dual frequency Coriolis mass flow meter. Proceedings of the North Sea Flow Measurement Workshop. https://nfogm.no/wp-content/uploads/2023/08/17-Multiphase-Metering-Using-a-Dual-Frequency-Coriolis-Mass-Flow-Meter_Aramco-_-Mahalingam.pdf

Nyholm, A., Arellano, Y., Liu, J., Krakowiak, D., & Salvo Rossi, P. (2026). Temporal data and short-time averages improve multiphase mass flow metering. arXiv preprint arXiv:2601.12433. https://arxiv.org/abs/2601.12433

Roshani, G. H., Nazemi, E., & Roshani, M. M. (2017). Flow regime independent volume fraction estimation in three-phase flows using dual-energy broad beam technique and artificial neural network. Neural Computing and Applications, 28(Suppl. 1), S1265–S1274. https://doi.org/10.1007/s00521-016-2784-8

Wang, L., Liu, J., Yan, Y., Wang, X., & Wang, T. (2017). Gas–liquid two-phase flow measurement using Coriolis flowmeters incorporating artificial neural network, support vector machine, and genetic programming algorithms. IEEE Transactions on Instrumentation and Measurement, 66(5), 852–868. https://doi.org/10.1109/TIM.2016.2634630

Zhang, Y., Liu, Y., Liu, Z., & Liang, W. (2019). Developing a long short-term memory-based signal processing method for Coriolis mass flowmeter. Measurement, 148, 106896. https://doi.org/10.1016/j.measurement.2019.106896

Zhu, J. H., Munjal, R., Sivaram, A., Paul, S. R., Tian, J., & Jolivet, G. (2022). Flow regime detection using gamma-ray-based multiphase flowmeter: A machine learning approach. International Journal of Computational Methods and Experimental Measurements, 10(1), 26–37. https://doi.org/10.2495/CMEM-V10-N1-26-37

الملخص

يُعدّ التحديد الدقيق لكثافة السائل النقي في أنظمة التدفق ثلاثية الأطوار (النفط والماء والغاز) تحدياً قياسياً متكرراً في إنتاج النفط والغاز. وتُقدّم تقنيات قياس نسب الأطوار التقليدية، كأجهزة قياس أشعة غاما المزدوجة، بيانات مرجعية موثوقة، غير أنها تنطوي على تكاليف باهظة ومخاطر إشعاعية وأعباء تنظيمية مرتفعة. تقترح هذه الدراسة إطاراً هجيناً مستنيراً بالفيزياء يعتمد على التعلم الآلي لتقدير كثافة السائل النقي، وذلك بالتنبؤ أولاً بنسبة الماء إلى السائل (WLR) باستخدام قياسات عداد تدفق الكتلة كوريوليس وكثافات الأطوار المشتقة معملياً فحسب، مما يُغني عن الحاجة إلى الأجهزة الإشعاعية. وتتمثّل المساهمة العلمية الجوهرية في اشتقاق معامل المتوسط التوافقي لكثافة الخليط (k_H)، وهو مؤشر لا بُعدي حسّاس للغاز يقيس الانحراف بين كثافة الخليط الحسابية والكثافة المتوسطة التوافقية للمنظومة ثلاثية الأطوار، مما يُمكّن نماذج التعلم الآلي من رصد سلوك التدفق المهيمن عليه بالغاز دون الحاجة إلى قياسه مباشرةً.

تضمّنت مجموعة البيانات 735,034 سجلاً تشغيلياً مُختوماً زمنياً، جُمعت من ثلاث وحدات اختبار منخفضة الأداء (LPT-A وLPT-B وLPT-C) المنتشرة عبر 26 بئراً نفطية في شركة دليل للبترول بسلطنة عُمان، وتغطي الفترة من يناير إلى أغسطس 2025. وقد طُبِّق تطبيع PVT وتصفية استقرار التدفق القائمة على الكميات المئوية والخالية من افتراض التوزيع قبل تدريب النموذج. وخضعت خمسة نماذج للتعلم الآلي للتقييم — الانحدار الخطي، وانحدار المتجهات الداعمة (SVR)، والغابات العشوائية، والتعزيز التدريجي، والشبكة العصبية الاصطناعية (ANN) — في ظل شرطين تجريبيين: تهيئة أساسية تعتمد فقط على مُدخلات مشتقة من كوريوليس (Q_l وρ_g)، وتهيئة كاملة تُضيف إليها k_H. وبدون k_H، أدّت جميع النماذج أداءً ضعيفاً ($R^2 \leq 0.194$)، مما يؤكد أن قياسات كوريوليس الخام وحدها غير كافية لتقدير WLR. وقد أسفرت إضافة k_H عن تحسّن متسق وجوهري في جميع النماذج الخمسة، إذ تراوح ΔR^2 بين 0.70+ و0.79+. وحقّق أفضل النماذج أداءً — الغابات العشوائية مع k_H — قيمة $R^2 = 0.8943$ وقيمة RMSE = 0.0854 على بيانات الاختبار المحجوبة. وتُقدّم هذه النتائج دليلاً تجريبياً قوياً على أن k_H هو المحرّك الرئيسي للدقة التنبؤية في هذا الإطار. ويُقدّم هذا النهج بديلاً فعّالاً من حيث التكلفة وخالياً من الإشعاع لقياسات اختبار الآبار في قطاع النفط والغاز العُماني.